Estudios Geológicos
enero-junio 2023, 79(1), e150
ISSN-L: 0367-0449
https://doi.org/10.3989/egeol.44775.621

A re-investigation on the historical cervantite-type antimony ochres

Reinvestigación de los ocres de antimonio históricos de cervantitas-tipo

Javier Garcia-Guinea[1,*], Fernando Gervilla[2], Fernando Garrido[1], Virgilio Correcher[3], Jose F. Marco[4], Laura Tormo[1].

[1]Departamento de Geología. Museo Nacional de Ciencias Naturales (MNCN), C/ Jose Gutiérrez Abascal 2. Madrid E-28006, Spain. ORCID ID: https://orcid.org/0000-0003-1848-3138, https://orcid.org/0000-0002-7491-3780, https://orcid.org/0000-0002-0581-2353

[2]Departamento de Mineralogía y Petrología e Instituto Andaluz de Ciencias de la Tierra (UGR-CSIC).. Facultad de Ciencias. Avenida Fuente Nueva S/N, Granada E-18071, Spain. ORCID ID: https://orcid.org/0000-0003-3592-9170

[3]Departamento Dosimetría Radiaciones. CIEMAT, Avenida Complutense 22, Madrid E-28040, Spain. ORCID ID: https://orcid.org/0000-0003-0864-6861

[4]Instituto de Química Física Rocasolano. C/ Serrano 119, Madrid E-28006, Spain. ORCID ID: https://orcid.org/0000-0002-5147-1449

*Corresponding author: Javier.Garcia.Guinea@csic.es

ABSTRACT

Antimony ocher are yellowish antimony oxo-hydroxides formed by weathering of stibnite (Sb_2S_3). They occur naturally as single crystallized phases in the isometric system with pyrochlore type structure, containing some Ca and water molecules in the structure, its range in composition can be expressed by the formula: $Sb^{5+}_{2-x}(Sb^{3+}, Ca)_y$ $(O, OH, H_2O)_{6-7}$, in which y is generally near 1, and x ranges from 0 to 1. Furthermore, Sb-ochres use to include substitutional As, Fe, Ta, Ti, Cu and others. This chemical variability keeping the structure has generated historical confusion of names of equivalent minerals with similar X-ray diffraction patterns being necessary the use of additional techniques. The mineral-type Cervantite from Cervantes (Spain) $(Ca, Sb^{3+})_2(Sb^{5+})_2O_6(OH)$ was disapproved at 1954 and re-approved at 1962 as α-Cervantite $Sb^{3+}Sb^{5+}O_4$ analyzing synthetic and natural antimony ochres from other localities, e.g., Brasina (Serbia) by X-ray diffraction. We herein characterize both historical specimens-type from Cervantes (Lugo, Spain) and Zajaca-Stolice (Brasina, Serbia) from the chemical-elemental, structural, thermal and speciation points of view, together with a vibrational study by Raman and FTIR, since the X-ray diffraction patterns of isometric samples with pyrochlore-type structure are excessively similar among them. The Cervantes specimen-type could be named hydroxycalciоromeite $(Ca, Sb^{3+})_2(Sb^{5+})_2O_6(OH)$ whereas the Brasina specimen-type $Ca_2(Sb^{5+})_4O_{12}(OH)_2$ is very similar but lacking Sb^{3+}; both specimens contain Ca and hydrous components, faraway of the official anhydrous orthorhombic α-Cervantite ($Sb^{3+}Sb^{5+}O_4$) setting. Micro-Raman was essential determining molecular phases and Sb-O bond vibrations, FTIR and DTA-TG finding hydroxyl groups and XPS defining Sb speciation.

Keywords*:* Cervantite; Romeite; Hydroxycalciоromeite; Specimen-type; Raman; XPS

Recibido el 2 de Agosto de 2022; Aceptado el 23 de enero de 2023; Publicado online el 11 de abril de 2023

Citation / Cómo citar este artículo: Garcia-Guinea, J. et al. (2022) A re-investigation on the historical cervantite-type antimony ochres. Estudios Geológicos 79(1): e150. https://doi.org/10.3989/egeol.44775.621

RESUMEN

Los ocres de antimonio son óxi-hidróxidos formados por meteorización de estibnita (Sb_2S_3). Normalmente aparecen como fases minerales simples cristalizadas en el sistema cúbico con estructura de tipo pirocloro y conteniendo algo de calcio y moléculas de agua en su red cristalina. Sus rangos composicionales pueden ser expresados por la fórmula: Sb^{5+}_{2-x} $(Sb^{3+}, Ca)_y$ $(O, OH, H_2O)_{6-7}$, donde $(_y)$ está cerca de 1 y $(_x)$ va de 0 a 1. También es muy frecuente que los ocres de antimonio incluyan sustituciones de As, Fe, Ta, Ti, Cu y otros. Esta variabilidad química dentro de la misma estructura ha generado confusiones históricas de nombres de minerales equivalentes con patrones de difracción de rayos X muy similares siendo importante complementar con técnicas analíticas adicionales. El mineral-tipo cervantita de Cervantes (Lugo, España) (Ca, $Sb^{3+})_2(Sb^{5+})_2O_6(OH)$ fue desacreditado en 1954 y re-aprobado en 1962 como α-cervantita $Sb^{3+}Sb^{5+}O_4$ difractando muestras de óxidos de antimonio sintéticos y naturales de otras localidades, como por ejemplo de Brasina (Serbia). En este trabajo estudiamos ambos minerales-tipo de Cervantes (Lugo, Spain) y de Zajaca-Stolice (Brasina, Serbia) desde los puntos de vista estructural, químico-elemental, termal, vibracional y de especiación química, asumiendo que los patrones de difracción de rayos X, los de la estructura tipo pirocloro son muy similares entre ellos. El espécimen tipo de Cervantes (Lugo) puede ser considerado como hydroxycalciоromeita $(Ca,Sb^{3+})_2(Sb^{5+})_2O_6(OH)$ mientras que el de Brasina $Ca_2(Sb^{5+})_4O_{12}(OH)_2$ es muy similar pero sin Sb^{3+}. Ambas muestras contienen calcio y componentes hidratados, es decir, ambos están lejos de ser la α-Cervantita ($Sb^{3+}Sb^{5+}O_4$) oficial anhidra y ortorrómbica. La espectroscopia micro-Raman es esencial para determinar fases minerales y vibraciones de enlaces Sb-O, mientras que espectroscopia FTIR y los ATD-TG fueron útiles para determinar grupos hidroxilos y aguas moleculares y la espectroscopia XPS para definir las especiaciones químicas del antimonio.

Palabras Clave: Cervantita; Romeita; Hydroxycalciоromeita; Especimen-tipo; Raman, XPS

Introduction

The extraction of antimony ores from stibnite (Sb_2S_3) and its subsequent burning produces valuable antimony oxides (Sb_2O_3 and Sb_2O_5) and Sb metal (Multani *et al*.,2016), but also acid mining drainage and potential pollution of toxic Sb to environment (Wilson *et al*., 2010). The element Sb forms a mixed-valence oxide, antimony tetroxide cervantite (Sb_2O_4), which includes both oxidation states of antimony Sb(III) and Sb(V). There is a growing demand for antimony compounds. Sb oxides are being used as flame retardants of polypropylene in increasing quantities (Li *et al*., 2012). Other antimony uses are to lead-acid batteries, plastics stabilizers and catalysts, ceramic and glass, bearings and solders, etc. (Corby, 2019). Antimonates are also frequently studied in ancient pigment compositions (Orecchio, 2013).

The pyrochlore super-group antimony oxo-hydroxide phases with isometric pyrochlore structure belong to romeite group, officially composed by fluornatroromeite, hydroxycalciоromeite, fluorcalciоromeite, oxycalciоromeite, oxyplumboromeite and probable stibioromeite and cuprorомeite pending to be studied (Atencio *et al*., 2010). Here, we focus our interest on the following minerals: (1) the new stibioromeite, formerly called the stibiconite, of Beudant (1837) defined then as antimony oxide containing water (wt.% 5.29); (2) the old lewisite, i.e., the new hydroxycalciоromeite (Burke, 2006); (3) the original romeite mineral was discovered by Damour (1841) in the Praborna mine (Piemont, Italy) and named in honor of French mineralogist Rome de l'Isle. This romeite-type specimen was initially defined as $CaSb_3+_2O_4$ and a speciation Sb5+ was later determined (Schaller, 1916), nowadays, romeite is discredited and the new mineral name accepted is named hydroxycalciоromeite $(Ca,Sb^{3+})_2(Sb^{5+},Ti)_2O_6(OH)$.

The intrinsic nature of the romeite subgroup minerals with (i) Ca, Sb, OH, some molecular H_2O and other accessory cations; (ii) an isometric pyrochlore-type structure; (iii) micro-granular colloform textures and (iv) some accessory paragenetic minerals, has created difficulties determining mineral species with many synonyms in the Ca-Sb-romeite group. For many years, these Ca-Sb-phases has been referred under two main names, stibiconite and cervantite, considering that stibiconite has priority (name suggested by Beudant, 1937), Vitalino & Mason (1952) recommend to drop the cervantite name from Cervantes (Lugo) (Dana, 1850). Accordingly, cervantite mineral was questioned and disapproved at 1954 by the International Mineralogical Association (IMA).

The mineral cervantite was re-approved by the IMA at 1962 as other different compound, the anhydrous orthorhombic α-Cervantite $Sb^{3+}Sb^{5+}O_4$ after the proposal of an experimental work performed by XRD of synthetic and natural antimony oxides from other new localities, e.g., Brasina (Serbia) (Gründer *et al*., 1962).

Modern facilities for identifying crystalline phases of small particle sizes are micro-XRD and micro-Raman techniques. The automatic search programs for both analytical techniques admit Boolean restrictions, i.e., selective searching's for chemical elements previously analyzed by the EDS probes. In our case, the romeite subgroup of Ca-Sb-bearing minerals shows very similar isometric pyrochlore-type crystalline structures hence the micro-XRD patterns must be supplemented with additional spectral and thermal techniques.

It was not until 1979, with the improved Raman technology when complete vibrational studies of antimony oxides were performed (Cody *et al*., 1979; Miller, 1982). Later, the Raman spectrum of a natural "α-cervantite" sample from Quebrada La Cebila (Rioja, Argentina) was published matching to other natural "cervantite-like" (i.e., stibiconite-stibioromeite) samples from Mexico, France and Brasina but not on the cervantite-type specimen from Cervantes (i.e., hydroxycalcioromeite) (Botto *et al*., 1990). Then, an extensive theoretical and experimental vibrational analysis of the Sb_4O_6 phase was performed in which the normal modes were decomposed into three non-redundant motions Sb–O–Sb stretch, Sb–O–Sb bend and Sb–O–Sb wag (Gilliam *et al*., 2004). Finally, Bahfenne & Frost issued three interesting vibrational spectroscopic studies on minerals of the calcium-romeite group: romeite (Italy) Bahfenne & Frost (2010a), lewisite (Switzerland) Bahfenne & Frost (2010b) and stibiconite (Mexico) Bahfenne & Frost (2010c) which are very similar to our "cervantite-type" specimens from Cervantes (Lugo) and Brasina (Serbia); being a good background for our vibrational study. Experimentally, we also detected stibnite relicts (Sb_2S_3) by micro-Raman since this phase has a characteristic spectrum limited to the 100-500 cm^{-1} region (Makreski *et al*., 2013; Kharbish & Jelen, 2016) and it is naturally weathered towards antimony oxo-hydroxides.

Taking into account this complex history, before proposing official changes in mineral nomenclature, we include here a previous characterization of the historical specimens-type of antimony ochres from Cervantes (year 1845) and Brasina (year 1962) by Bulk and micro-X-Ray Diffraction (XRD), Environmental Scanning Electron Microscopy with Energy Dispersive Spectrometer and Cathodoluminescence Detectors (ESEM-EDS-CL), Field Emission Scanning Electron Microscopy (FE-ESEM) with Qemscan; Differential Thermal Analysis and Thermogravimetry (DTA-TG) and X-ray Photoelectron Spectrometry (XPS) together with a vibrational study by Laser Micro-Raman Spectroscopy (LRS) and Fourier Transformed Infrared Spectrometry (FTIR).

Materials and methods

Samples. - Two historical specimen-types were officially used by the International Mineralogical Association (IMA) to name, to discredit and to re-approve the cervantite mineral (Sb_2O_4) (Fig. 1). The first one was collected by Mr. Vallejo from Cervantes town (Lugo, Spain, 1844), analyzed then as hydrous calcium antimony oxide, and stored (nº 18269) in the Mineralogical Collection of the National Museum of Natural Sciences of Madrid. The second specimen-type stems from the Zajaca-Stolice district, Brasina, Serbia (nº 4986, legacy Prof. Gründer, 1961 stored in the Mineralogische Sammlungen Technische (Universität Berlin) (Gründer *et al*., 1962). This same Serbian specimen was used to re-establish the cervantite mineral specie as valid mineral from the IMA (Dana, 1850). For the present study, a sample portion was gently provided by curator Dr. Susanne Herting-Agthe from the Berliner museum (Fig.1).

X-Ray Diffraction.- The resultant XRD profiles of the bulk (powdered sample) Cervantite-type specimens were studied by XPOWDER software performing background subtraction, K2 stripping and chemical elements restrain as the most abundant and representative elements previously detected in the yellowish-brown masses (Martin, 2006). This software package allows a full

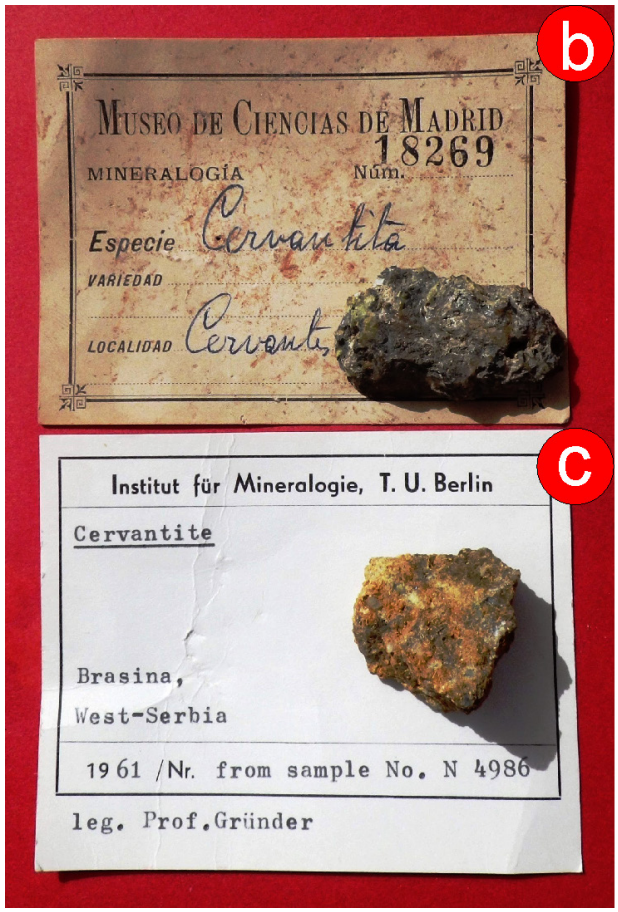

Figure 1.— Historical cervantite specimen-types stored in the Museo Nacional de Ciencias Naturales (Madrid). Both samples were officially used by the International Mineralogical Association (IMA) to name, discredit and re-approve the cervantite mineral (Sb_2O_4)

duplex control of our Philips PW-1710/00 diffractometer (MNCN, CSIC) using a broad focus X-ray tube for Cu Kα radiation with a Ni filter and a setting of 40 kV and 40 mA. The qualitative search-matching procedure was based on the ICDD-PDF2 database and the DIFDATA free database of the RRUFF Project. The software uses Boolean searching and chemical restraints to elements previously detected by other techniques such as EDS, e.g., Sb, O and Ca. In addition, the spatially-resolved micro-XRD measurements were recorded on the mineral sliced surfaces at open air and room temperature using a Bruker D8 Discover high-resolution X-ray diffractometer, Gobel mirror, four bounce germanium monochromator and a scintillation detector. This technique permits performing structural analyses on micro-cluster areas obtaining experimental patterns, for instance, matching on the PDF Cards 11-694 (Cervantite) and 73-1736 (Romeite).

Electron Microscopy. - Both historical yellow masses of antimony ochres were analyzed in the Spanish Centers for Scientific Instrumentation of Madrid (MNCN-CSIC) and University of Granada (CIC-UGR).

The environmental scanning electron microscope ESEM-EDS-CL, FEI Inspect Company, MNCN, Madrid, was used to record morphology images, chemical-elemental composition and cathodoluminescence spectra. This ESEM facility can operates in low vacuum conditions, analyzing as received samples avoiding experimental coatings onto sample, this last feature is required to allow the cathodoluminescence emission exit from the sample inside. The ESEM resolution operating at low-vacuum was at 3.0 nm/30 kV (SE), 4.0 nm/30 kV (BSE) and <12 nm/3 kV (SE). The accelerating voltage was at 30 kV and the probe current up to continuously adjustable 2 mA. We also operated with a backscattered electron detector (BSED) under vacuum conditions of 30 Pa, at high voltage of 20 kV, a suitable beam spot diameter for particular magnifications and a working distance of approximately 10 mm to the detector. The chemical-elemental microanalyses (EDS) were performed with an energy-dispersive X-ray spectrometer (INCA Energy 200 energy dispersive system). The software used for the quantification was Microanalysis Suite, INCA suite version 4 (Oxford Instruments). This ESEM has a coupled MONOCL3 Gatan probe to record cathodoluminescence (CL) spectra with a PA-3 photomultiplier. The photomultiplier tube covers a spectral range of 185–850 nm being more sensitive in the blue region of the spectrum. A retractable parabolic diamond mirror and a photomultiplier tube were used to collect and amplify the luminescence emission. The sliced samples were positioned 16 mm beneath the bottom of the CL mirror assembly. The excitation voltage for CL measurements was delivered at 25-kV electron beam.

In the Center for Scientific Instrumentation (CIC) of the Granada University we used an environmental scanning electron (ESEM) microscope (Quanta 400 by Thermofisher-FEI with EDS XFlash by Bruker, equipped with a XFlash 6/30 detector) and

a field-emission environmental scanning electron (FE-ESEM) microscope (Qemscan 650FEG by Thermofisher-FEI with Dual EDS XFlash by Bruker, equipped with a XFlash 6/30 detector) for quantitative evaluation of minerals. These facilities allow collecting QEMSCAN data in field scan mode providing full images of each field of the sample block, giving both qualitative major element chemical maps and a mineral phase map of the full thin section.

Differential Thermal and Thermogravimetric Analyses. - The DTA-TG analyses of 10±0.10 mg of grinded specimens were recorded with a STA 6000 Simultaneous Thermal Analyzer of PerkinElmer in N_2 atmosphere operating under powerful Pyris™ software control. Samples were carefully prepared, crushed in an agate mortar to particle size less than 2 mm discarding the fraction less than 100 mm to minimize the effects of absorbed water. Thermal treatments were performed at a heating rate of 10°C min^{-1} from room temperature up to 950°C. Powdered samples were held in a platinum crucible with alumina which also acted as stable reference material.

Micro-Raman and Photoluminescence. - The Raman-PL spectra of the specimens-type were recorded with a Thermo-Fisher DXR Raman microscope (West Palm Beach, FL 33407, USA) with a point-and-shoot Raman capability of 1-µm spatial resolution using a laser source at 532 nm. We used the 100X objective of the confocal microscope together with a 532 nm laser source delivering 10mW at 100% laser power mode. The average spectral resolution in the Raman shift, ranging from 100 to 5000 cm^{-1}, was 4 cm^{-1}, with 900 lines·mm^{-1} grating and 2 µm spot size. The system was operated with OMNIC 1.0 software using as pinhole aperture of 25 µm, bleaching time 30 s; average of four exposures timed 10 s each.

Fourier Transformed Infra-Red Spectroscopy. - The FT-IR spectra of yellow-translucent particles of the historical specimens were measured in a Thermo-Scientific Nicolet iN10 FT-IR Microscope attached to a Nicolet iZ10 FT-IR unit, which allow measurements of samples sized few microns. These particles were analyzed with a slide-on germanium tip-ATR crystal of high sensitivity specific for small particles. Spectra were collected in 8 seconds using OMNIC 1.0 software which combines infrared microanalysis and spectral identification. The system also records line-scan and chemical maps in automatic mode.

X-Ray Photoelectron Spectrometry. - The XPS measurements of sliced samples were performed in a home-made multipurpose ultra-high vacuum chamber equipped with a dual Mg/Al anode and a Phoibos 150 hemispherical analyzer. The XPS data were acquired using Al Kα radiation (hν = 1486.6 eV). The spectra were recorded at an electron take-off angle of 90º with constant analyzer pass energy of 100 eV for the wide energy range scan and with pass energy of 20 eV for narrow scan spectra. All binding energies are referred to the main C_1s signal of the adventitious carbon layer, which was set at 285.0 eV. The spectra were analyzed using the Casa XPS software.

Results

X-ray diffraction analyses

Powder method. - The chemical restriction to Ca-Sb-O elements improved the Boolean search-matching on the ICDD-PDF2 and RRUFF databases suggesting three PDF2 card files: (1) 73-1736 (romeite $Ca_2Sb_2O_7$); (2) 32–0263 (muscovite $KAl_2(Si_3Al)O_{10}(OH,F)_2$) and 46-1045 (α-quartz SiO_2). The three cards match all XRD peaks of the experimental XRD profiles (Fig. 2). The reference intensity ratios parameters (RIR) of these patterns together with chemical data allow performing semi-quantitative XRD analyses point to romeite species with accessorial amounts of quartz and muscovite. The refined cell parameters of both cervantite-type specimens were calculated by least squares fitting. The experimental unit cell dimensions of the Cervantes-yellow-mass are as follows: a_o = 10.282, b_o = 10.282 and c_o = 10.282, α=β=γ=90; cell volume 30.846$Å^3$, group Fd-3m, CuK_α=1.5418 and for the Brasina-yellow-mass the parameters are: ao = 10.253, bo = 10.253 and co = 10.253, α=β=γ=90; cell volume 30.759$Å^3$, group Fd-3m CuKα=1.5418. Considering the small size of the cervantite-type (hydrous Ca-romeite) crystals observed in the optical measurements, we determined the size of the coherent domain and the strain analysis of sample by the Williamson-Hall method from the experimental XRD profiles. The diffracted intensity of an X-ray beam in the Fourier space has

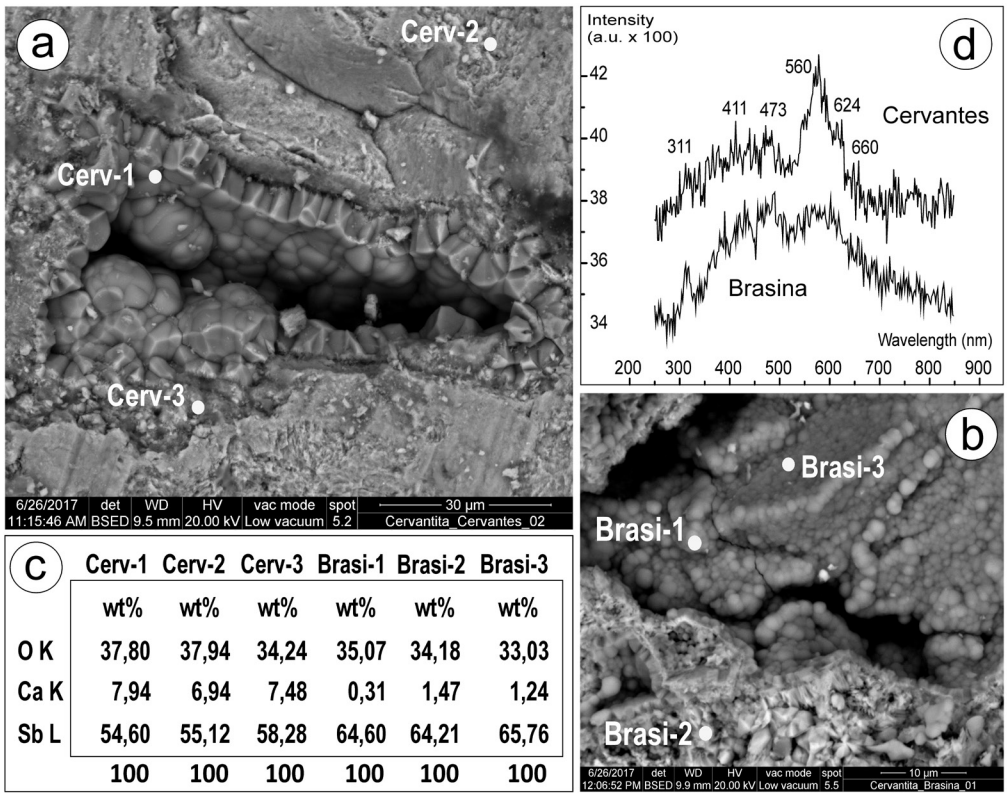

c

	Cerv-1	Cerv-2	Cerv-3	Brasi-1	Brasi-2	Brasi-3
	wt%	wt%	wt%	wt%	wt%	wt%
O K	37,80	37,94	34,24	35,07	34,18	33,03
Ca K	7,94	6,94	7,48	0,31	1,47	1,24
Sb L	54,60	55,12	58,28	64,60	64,21	65,76
	100	100	100	100	100	100

Figure 2.— X-ray diffraction profiles of the bulk (powdered sample). Qualitative search-matching based on ICDD-PDF2 and RRUFF databases using Xpowder software with Boolean searching and chemical restraints to elements detected by EDS, e.g., Sb, O and Ca. Experimental samples match on Romeite 73-1736 XRD Card.

been considered by the profile deconvolution of the structural line to define the space dispersion (Δd/d%). This area weighted method establishes that absolute values of Fourier-cosine coefficients are product of the size and strain coefficients. Accordingly, for the Cervantes yellow mass case we obtain a coherent domain size of 26.25±0.00 nm and non-uniform strain (%) of 0.162±0.00 and for the Brasina yellow mass case a coherent domain size of 17.20±0.00 nm and non-uniform strain (%) of 0.00±0.00. Both experimental bulk XRD profiles of the Cervantite-type specimens fit well into romeite crystallographic lattices; furthermore, the calculations of cell parameters, crystallite size and strain stand up subtle structural differences among them.

Micro-Diffraction Method.- This second XRD method allows focus the analysis on small micrometric areas measuring many spots to check potential structural variabilities of the phase studied in the rock section. We selected yellow whitish zones, characteristic of antimony ochers, observing a common XRD pattern of the romeite subgroup minerals for both samples. The five strongest XRD lines detected in all experimental profiles are 3.11(m) (311); 2.96(s)(222); 2.56(m)(400); 1.81(ms)(440); 1.55(ms)(622) they agree with the general features of the members of the pyrochlore super-group. The XRD patterns of the Cervantes specimen-type match on PDF-XRD cards 7-66 lewisite, $(Ca,Fe,Na)_2(Sb,Ti)_2(O,OH)_7$; 10-388 stibiconite $Sb_3O_6(OH)$ and 73-1736 romeite ($CaSb_2O_7$), all phases included in the romeite sub-group of the pyrochlore super-group of minerals (Atencio *et al*., 2010) being not possible to match experimental XRD measurements of Cervantes specimens-type into PDF cervantite cards, e.g., 11-694. Both sets of XRD profiles (Cervantes & Brasina specimens) display little structural differences among them. Remarkably, we performed a good matching of one experimental micro-XRD profile (Brasina-N4) on the PDF Card 11-694 (cer-

vantite) however other recorded Brasina micro-XRD profiles match better on mixtures of stibiconite-cervantite or lewisite PDF cards.

ESEM-EDS-CL and FESEM-QEMSCAN analyses

The electronic images recorded on yellow masses from Cervantes and Brasina samples (Figs. 3a & 3b) show structures of precipitation of minerals in aqueous and gaseous systems circulating through fissures. In the samples images, botryoidal textures and abundant cavities were observed. The EDS spot analyses point to antimony oxides with variable amounts of Ca in formula. In addition, they contain accessorial amounts of Pb, As, Fe, P, Al and Cu (Table 1).

It is important to note that Cervantes sample exhibit frequent amounts of Ca averaging circa 7%. Conversely, Brasina specimen shows amounts of Ca averaging circa 1% (Fig. 3c). CL spectra of specimens, depicted in Fig. 3d, exhibit frequent low intense wavebands at circa 311, 411, 473, 560, 624 and 660 nm. The CL spectral profiles do not exhibit strong luminescent centers as many other hydrous minerals with low luminescence emission. Phase assemblage maps of FESEM-QEMSCAN mineral identification were also performed for the antimony ochre specimens. These images of mineral phases stem from elemental compositions combined with back-scattered electron brightness and X-ray count rate information (Gottlieb *et al*., 2000). We observed Sb-bearing minerals galena, muscovite, apatite, quartz and calcite in both samples. The Cervantes specimen has additional iron oxo-hydroxide layers and other Ti and Fe sulphates phases. The abundance of mineral species

Table 1.—Chemical-Elemental analyses of antimony ochres from Cervantes (Spain) and Brasina (Serbia)

Table 1.- ESEM Chemical-Elemental Analyses									
Elem	Cerv-4	Cerv-5	Cerv-6	Cerv-7	Cerv-8	Cerv-9	Brasi-4	Brasi-5	Brasi-6
	wt%	wt%	wt%	wt%	wt%	wt%	wt%	wt%	wt%
S K	0	0	0	0	0	0	0,48	0	0
C K	1,89	0	2,17	0	0	3,03	0	0	0
O K	26,71	25,73	25,52	25,33	26,74	25,79	33,62	32,73	33,31
P K	0	0	0	3,13	0	0	0	0,63	0
Cl K	0	0	0	1,75	0	0	0	0	0
Al K	0	0,36	0,37	0	1,4	1,13	0	0	0
Si K	1,35	1,22	0,65	0	0	1,46	0,93	4,27	1,28
Ca K	7,44	6,94	7,6	2,43	0	2,78	2,21	6,22	1,34
Sb L	62,61	65,75	63,69	18,54	53,59	43,64	62,76	54,76	62,97
As L	0	0	0	3,94	1,5	1,15	0	1,39	1,1
Pb M	0	0	0	44,88	0,75	18,93	0	0	0
Cu K	0	0	0	0	1,01	0	0	0	0
Fe K	0	0	0	0	15,01	2,09	0	0	0
Totals	100	100	100	100	100	100	100	100	100

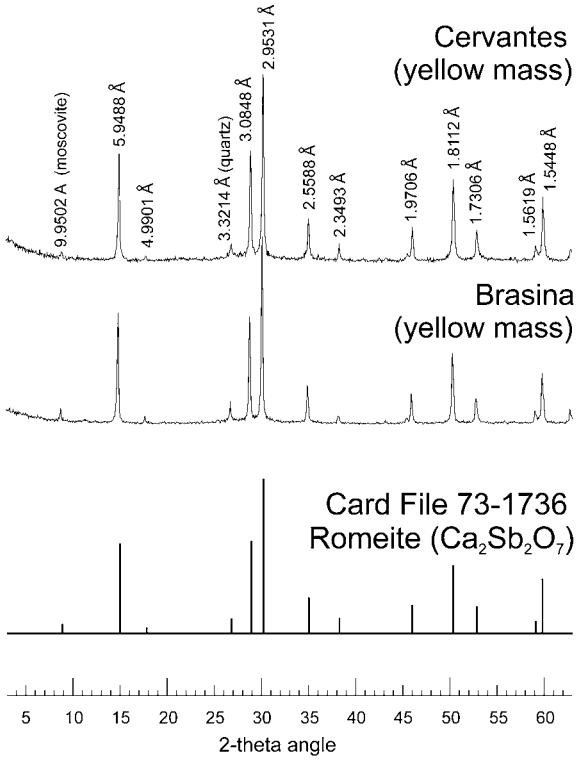

Figure 3.— Environmental Scanning Electron Microscopy: (a) Botryoidal textures of hydroxycalciоromeite admixtures in a cavity (Specimen-type from Cervantes, Spain). (b) Botryoidal textures of hydroxystibioromeite admixtures in a cavity (Brasina, Serbia). (c) Simplified Chemical-Elemental spot EDS analyses, (d) Spectral cathodoluminescence emissions linked to hydroxyl and water groups.

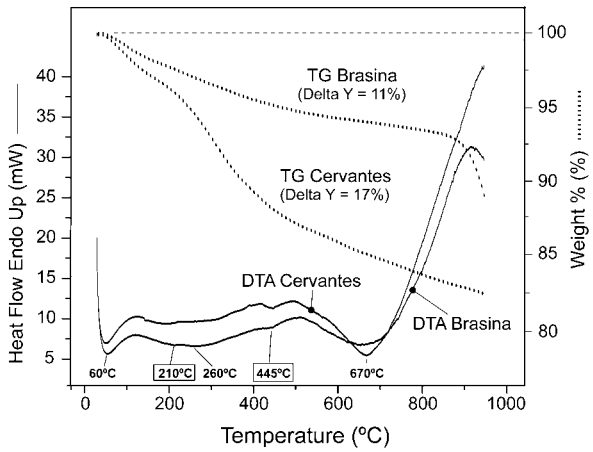

Figure 4.— DTA-TGA analyses of antimony ochres samples in N_2 atmosphere at a heating rate of 10°C min^{-1} from RT up to 950°C. Brasina sample show a thermal loss of 11% and Cervantes 17%.

and its textural complexity make it difficult extracting pure antimony oxides to perform bulk analyses

Differential Thermal and Thermo-gravimetric analyses

The DTA/TG curves of both Sb-ochre specimens can be observed in Fig. 4. The two endotherms effects appearing in the DTA curves peaked at 60ºC and finishing at circa 120ºC can be associated with water weakly bonded to the structure, i.e., adsorbed or absorbed water. Next, it is interesting to note other two little endotherms at circa 210ºC and 445ºC in both samples, probably associated with dehydroxylation processes from precursor Sb-OH or Ca-OH bonds, characteristic of romeite specimens. The total weight losses obtained by thermo-gravimetry are 11% (Brasina) and 17% (Cervantes) is another additional feature helping to separate both antimonates. The endothermic DTA peak at circa 670ºC can be probably interpreted as the starting point of the Sb_2O_3 formation reaching a maximum at the exothermic peak sited circa 920ºC.

Vibrational spectroscopy

Yellow masses of Cervantes sample show noisy and low intense Raman spectra with a detached main peak at circa 514 nm matching roughly on other romeite and lewisite Raman spectra (Fig. 5a). The yellow masses of the Cervantite-type from Brasina display a more intense Raman spectrum with a main band at 199 cm^{-1} and lower intensity bands at 146, 400, 461 and 422 cm^{-1} (Fig.5a). Such spectrum is comparable with other Raman spectra of stibiconite, e.g., Yacunani Mine Tejocotes (Oaxaca, Mexico).

The FTIR bands in both yellow specimens, from Cervantes and Brasina sites, as many other antimony oxides, are observed in the 400-1000 cm^{-1} spectral region and other two bands peaked at 1638 and 3452 cm^{-1} linked to hydrous components. Both also display characteristic Sb-O deformation modes of antimony oxides at 731 cm^{-1} and 552 cm^{-1} (Fig. 5b).

X-ray photoelectron spectrometry

The wide scan XPS spectra recorded from Sb-ochre samples Cervantes and Brasina exhibits intense signals which correspond to various electron core levels

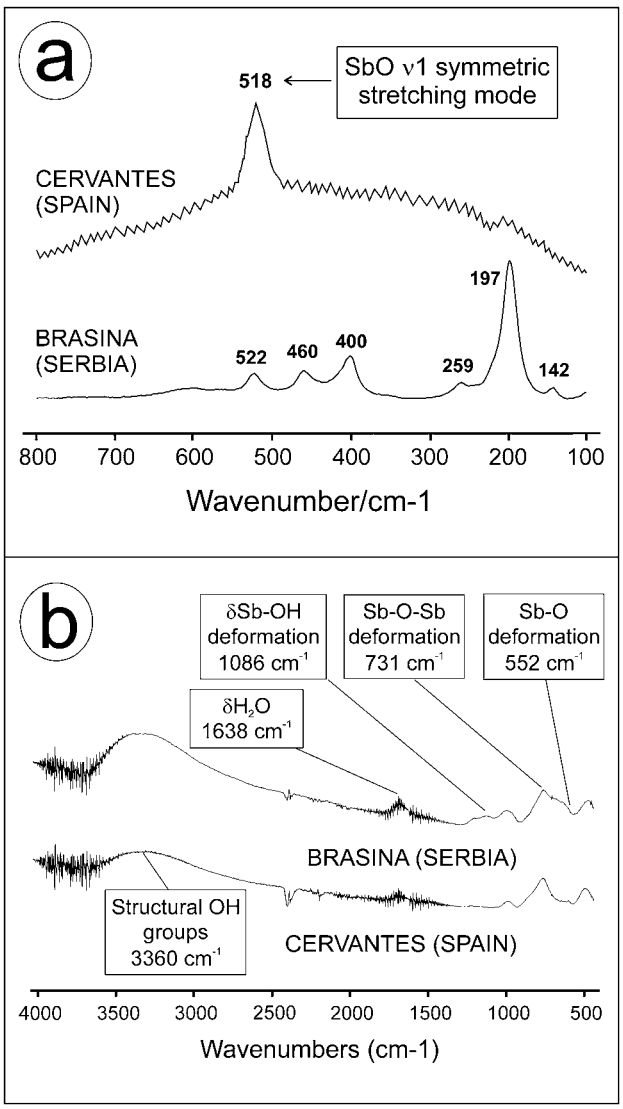

Figure 5.— Vibrational spectra of Cervantes and Brasina antimony ochre specimens: **(a)** Laser (532 nm) Raman Spectra. Note as the lack of multiple bands in Cervantes sample provides evidence for the equivalence of SbO units in the romeite molecular structure. Brasina spectrum exhibits multiple bands of different SbO units. **(b)** Similar FTIR spectra of Cervantes and Brasina. Structural hydroxyl groups' broad band and little molecular water peaks are observed in addition to the SbO deformation bands.

of Sb. In addition, Cervantes ochre contains C, Ca, Si, Al, Pb, Fe, Ti and N contributions. The O 1s main core level overlaps completely with the Sb $3d_{5/2}$ peak and its contribution cannot be separated from the later in a low resolution, wide scan spectrum. The Brasina ochre has a less complex composition. Besides the Sb (and oxygen) contributions, it shows C, Ca, Si, Ti and N contributions. The chemical composition determined by XPS (which refers to the outermost 5 nm of the sample) correlates well with that found by ESEM-EDS-CL and FESEM-QEMSCAN analyses.

The C1s core level spectra recorded from both samples are very similar. They contain three different components located at the binding energies (BEs) of 285.0 eV, 286.7 eV and 288.8 eV. These components can be associated to different organic functional groups as C-C, C-O and C=O, respectively (Báez *et al*., 2017).

The chemical state of Sb can be identified from the analysis of the Sb 3d core levels. However, as mentioned above, the O 1s core level peak overlaps completely with the main Sb $3d_{5/2}$ one and this complicates somehow such identification. Fortunately, the Sb $3d_{3/2}$ peak is completely separated and, using a rigorous fitting procedure, the position and area of the Sb $3d_{5/2}$ peak can be determined since: (i) the spin-orbit separation between the two peaks is known to be 9.4 eV (Garbassi, 1980), (ii) being 3d core levels, the area ratio between the two components of the Sb 3d spin-orbit doublet is fixed by the multiciplity of the corresponding electron states, i.e.,

$$(2j\_1+1)/(2j\_2-1)=(2\cdot 5/2+1)/(2\cdot 3/2+1)=6/4=1.5$$

and (iii) the line width of the two Sb 3d peaks has to be equal. Using these constraints plus the additional, usual one, of fixing the linewidth of the different oxygen states to be the same we obtain the fits presented in Fig. 6.

Besides the Sb $3d_{5/2}$ core level peak there are three different oxygen contributions under the Sb $3d_{5/2}$+O 1s envelope which are located at 529.5 eV, 531.2-531.9 eV and 533.4-533.9 eV. While the first one has an unequivocal assignment (it corresponds to metal-oxygen bonds) (Marco *et al*., 2004), the second and the third components can be associated to various oxygen chemical species. For example, components in the range 531.2-531.9 eV can be associated to oxygen in surface oxygen defective sites and hydroxyl groups (Marco *et al*., 2004), alumina (Smirnov *et al*., 2007), Si-O bonds (Meskinis *et al*., 2020) or organic oxygen (López *et al*., 1991), while components in the range 533.4-533.9 eV can be associated to a multiplicity of chemically- and physically-adsorbed water

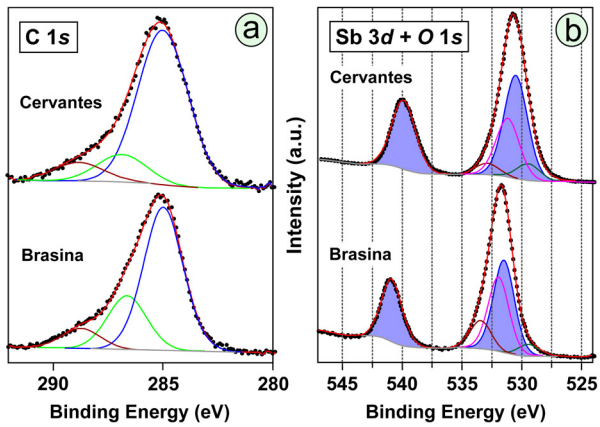

Figure 6.— **(a)** C 1s narrow scan X-ray photoelectron spectra recorded from Cervantes and Brasina samples. **(b)** Sb 3*d* and O 1*s* narrow scan spectra recorded from the Cervantes and Brasina samples. The Sb 3d spin-orbit doublet is shown in solid light blue color.

(Marco *et al*., 2004) or other organic oxygen groups (López *et al*., 1991). These contributions are difficult to disentangle and an increase or decrease in their intensity cannot be associated in an unequivocal way to an increase or decrease in the concentration of a particular oxygen species in the present case.

The BE of the Sb $3d_{5/2}$ core level in the Cervantes and Brasina samples is quite different (530.7 eV and 531.6 eV, respectively). This large difference of 0.9 eV is a clear indication of the different oxidation state of antimony in both samples. Table 2 collects literature values for the BE of the Sb $3d_{5/2}$ core level for various oxidation states of antimony (Antimony XPS URLs; Bodenes *et al*., 2015; Birchall *et al*., 1975; Delobel *et al*., 1983; Morgan *et al*., 1973).

Inspection of Table 2 strongly suggests that antimony is present in the Brasina sample exclusively as Sb^{5+} while it exists as Sb^{4+} in the Cervantes sample. This oxidation state of "Sb^{4+}" most probably reflects the coexistence of Sb^{3+} and Sb^{5+} as it can be expected for a stibiconite-type mineral (Stevens *et al*., 1993). We would like to recall that the BEs of the Sb 4p core levels in the Cervantes and Brasina samples (not shown) are 35.0 eV and 35.6 eV, respectively, what supports the oxidation state assignments made above (Izquierdo *et al*., 1989).

Long time ago it was shown by Mössbauer spectroscopy (Stevens *et al*., 1993) in a series of stibiconite samples that there exists a correlation between the Ca content of the minerals and the Sb^{3+}/Sb^{5+} ratio:

Table 2.— Literature values collected for the binding energy of the Sr 3d5/2 core level in different antimony oxides (referenced to the C 1s BE of 285.0 eV; all the values are given in eV).

Sb_2O_3	Sb_2O_4	Sb_2O_5	Reference
530.1	--	531.5	Wagner et al., (2003)
530.1	--	531.1	Moulder et al. (1992)
531.0	--	--	Bodenes et al., (2015)
530.2	530.7-531.2	531.1	Birchall et al., (1975)
530.3	530.5	531.1	Garbassi (1980)
530.3	530.9	531.2	Izquierdo et al., (1989)
530.4	530.6	531.0	Delobel et al., (1983)
530.0	--	530.8	Morgan et al., (1973)

lower Ca percentages imply larger Sb^{3+} contributions while Sb^{5+} rises with increasing Ca concentrations. This correlation, however, is not observed here since these particular samples contain similar amount of Ca and, despite this, they show important differences in the Sb oxidation state.

Discussion

Centimetric mineralized quartz veins with Sb-Pb-Fe sulphides of Cervantes (Lugo, Spain) are hosted in metamorphic slate rocks. The local climate is warm-humid, circa 1300 mm/year, providing raining water enough for the Sb phases weathering. In such environments, the inorganic oxidation state of antimony Sb(V) use to be the common state of the Sb element. Sb(V) is the oxidation state for acid pH's of oxygenated waters coming from sulfides weathering is $Sb(OH)^{6-}$, the deprotonated form of antimonic acid, which reacts with surrounding cations, e.g., Fe, Ca, Pb, Ti, Cu, etc. Antimony Sb(V) ions are easily adsorbed onto α-Fe_2O_3 surfaces at circa pH 4 from aqueous solutions (Ambe, 1987).

The five strongest XRD lines observed in all experimental profiles (Fig. 2) agree with general features of members of the pyrochlore super-group minerals. In our measurements, XRD patterns of the Cervantes specimen-type match on PDF-XRD cards 7-66 Lewisite, $(Ca,Fe,Na)_2(Sb,Ti)_2(O,OH)_7$; 10-388 Stibiconite $Sb_3O_6(OH)$ and 73-1736 Romeite ($CaSb_2O_7$), all these phases are included in the romeite sub-group

of the pyrochlore super-group of minerals (Corby, 2019) being not possible to match experimental micro-XRD measurements into the Cervantite card 11-694. However, some little areas of the Brasina sample display a good matching on such PDF Card labelled as Cervantite, e.g., spot Brasina-N4 but other Brasina micro-XRD profiles match better on mixtures cervantite, stibiconite and lewisite PDF cards. This sample from Brasina is exactly the same historical specimen used by Prof. Gründer (Gründer *et al*., 1962) for the re-approval of the "Cervantite" mineral as a Sb_2O_4 anhydrous oxide (Servos, 1962). This feature explains perhaps why Brasina specimen-type is somewhat more anhydrous than the Cervantes specimen-type. Nowadays, the old type specimen "lewisite" (Hussak & Prior, 2018) is considered as hydroxycalciоromeite in according to the lewisite crystal recent structure determinations (Rouse *et al*., 1998; Zubkova *et al*., 2000). It is important to note that the oxycalciоromeite $Ca_2Sb_2O_6O$, from Buca della Vena mine (Tuscany, Italy) (Biagioni *et al*., 2013) is other member of the pyrochlore supergroup also displaying the five strongest lines observed in all our experimental XRD profiles (Fig. 2).

Under the ESEM & FESEM microscopes we observed iron oxide layers in the Cervantes sample. The most relevant data to our concern are that many EDS-spots of Sb-areas of the Cervantes sample exhibit frequent amounts of Ca, averaging circa 7% while Brasina specimen's displays Ca amounts averaging circa 1% (Fig. 3). In addition, the EDS analyses of yellowish phases show oxygen percentages ranging from 25 up to 38 wt.% and Sb ranging from 54 up to 66% wt.% which point to Ca-Sb-oxo-hydroxide phases, e.g., oxycalciоromeite or hydroxycalciоromeite. The ESEM-CL peaks (Fig. 3d) observed at circa 315, 620 and 650 nm peak groups can be associated with hydrous molecules from variated origins such as structural, absorbed, adsorbed or environmental water (Garcia-Guinea, *et al*. 2018). Concerning the observed main cathodoluminescence band at circa 560 the proposed mechanism consists of a non-specific reaction electron-beam + 2 (Metal-OH)>H_2O + O + photons that agrees with radiolytic models analyzing luminescence emission of hydrous materials (Garcia-Guinea *et al*. 2017). Finally, the blue emissions peaked in the 410-420 and 460-480 nm CL spectral regions could be due to the radiative recombination of self-trapped excitons (STE) because of the radiolysis of oxygen bonds (Stevens-Kalceff & Phillips, 1995). In summary, the CL spectra of both samples suggest the occurrence of hydroxyl groups and water molecules, but in greater quantities in the Cervantes sample compared to Brasina one. The FESEM-QEMSCAN map shown complex phase assemblage maps of both specimen surfaces, in the Cervantes case, corresponding to a former mineralization of quartz veins of Sb-Pb-Fe sulphides with clear later weathering traces.

The TG-DTA curves for both powdered romeite samples, under nitrogen atmosphere, are shown in (Fig. 4). Thermogravimetric curves display total weight losses of 11% (Brasina) and 17% (Cervantes) which could be explained by dehydration and dehydroxylation thermal mechanisms. The first endothermic peak from 60ºC to 110ºC must be attributed to a little amount of molecular water vaporization. Later, at higher temperatures, the dehydroxylation features can be observed at different temperatures, for example, endothermic peaks at 210ºC, 260ºC, 445ºC and 670ºC up to a complete decomposition of $Sb(OH)_5$ to Sb_2O_5 and H_2O. The thermal decomposition must have ended totally with the exothermic DTA at circa 860ºC (Fig. 4). After 400°C, we do not observe the possible weight gain when Sb^{3+} is oxidized to Sb^{5+} (Abdel-Galil *et al*., 2015).

From the molecular approach of the laser micro-Raman spectroscopy, the yellowish areas of the Cervantes specimen-type display high matching grades with romeite RRUFF card files and the Brasina specimen-type with stibiconite and cervantite RRUFF card files (Fig. 5a). The antimonates stibiconite $SbSb_2O_6(OH)$ and romeite $Ca_2Sb_2O_6(OH,O)$ are isostructural phases (F d3m 4/m $\bar{3}$ 2/m) with other pyrochlore-group minerals of general formula $A_2{-}mB_2X_6{-}wY_1{-}n{\cdot}pH_2O$. Romeite specimens admit a wide range of independent substitutions on the A- and B-sites and coupled substitutions among the A- and B- and between the A- and Y- sites (Atencio *et al*., 2010). The micro-Raman spectra of the Cervantes yellowish spots frequently exhibit only a large peak at circa 517 cm^{-1} which are assigned to the SbO ν1 symmetric stretching mode. It is important to note that the lack of multiple bands in the Raman

spectrum provides evidence for the equivalence of SbO units in the romeite molecular structure (Miller & Cody, 1982). These Sb-O bond vibrations are also observed in other natural and synthetic antimonates (Fig. 5a). The Cervantes romeite micro-crystalline sample display from 5% to 9% of Ca in all our experimental EDS spots hence, it's quite likely its incorporation into the romeite crystal lattices along with some other surrounding cations such as Fe or Ti, with a possible approaching to the formula (Ca, Fe,)$_2$(Sb^{5+}, Ti^{4+})$_2$(O,OH)$_7$. In addition, we do not observed the strong Raman band at 1092 cm^{-1} associated to CO_3 group's vibration of calcium carbonates (Gunasekaran *et al*., 2006). Conversely, the Brasina micro-Raman spectra of the yellow spots looks different, they are more similar to those others published on the Cervantite and Stibiconite specimens showing several Raman peaks (Fig 5a). These are phases poorer in Ca (Brasina only shows 1 or 2 wt. % Ca) and richer in Sb displaying an intense Raman emission at circa 200 cm^{-1} and associated peaks at 145, 220, 250 and 260 cm^{-1} (Fig 5a). Raman bands for synthetic oxides of antimony are also observed among 145 and 260 cm-^{1} (Cody *et al*., 1979) According to the DFT calculations of (Bahfenne & Frost, 2010a) the most prominent emission at 199 cm^{-1} band of stibiconite is assigned to O-Sb-O bending modes. Stibiconite could contain some Ca and H_2O with a most realistic formula (Sb^{3+}, Ca)$_y$ Sb^{5+}_{2-x} (O,OH,H_2O)$_{6-7}$ where y approaches 1 and x varies from 0 to 1. The infrared spectra in both specimens from Cervantes and Brasina (old lewisite vs new hydroxycalciomeite) ore deposits are very similar. The broad band peaked circa 3360 cm^{-1} (Fig 5b) is the OH stretching region associated to structural OH groups (Rouse *et al*., 1998). FTIR peaks located in the spectral region from 963 to 1196 cm^{-1} can be assigned to SbOH deformation modes (Bahfenne & Frost, 2010c). Mostly intense is the 731 cm^{-1} band attributed to SbO antisymmetric stretching vibrational mode also observed in antimony pentoxide (Sb_2O_5) (Bahfenne & Frost, 2010c), Brasina sample displays a small band observed circa 1086 cm^{-1} (Fig 5b). Concerning the molecular water item, the FTIR band observed at 1638 cm^{-1} is associated to water bending modes (Bahfenne & Frost, 2010c), accordingly, there may be either adsorbed or involved molecular water in the structure. Finally, the spectral region from 600 to 900 cm^{-1} was traditionally assigned to SbO stretching vibrations (Gadsen, 1975; Siebert, 1959). Brasina sample display a tiny 552 cm^{-1} band assigned to SbO deformation associated with Sb^{3+} valence state but not observed in the Cervantes sample case (Fig 5b).

Antimony oxides Sb_2O_3, Sb_2O_4, Sb_2O_5 can be separated among themselves by XPS, since this technique provides crucial information on the elemental stoichiometry and chemical state of their surfaces. The Cervantes primary hydrothermal mineralization is composed by Stibnite (S_2S_3), a phase detected by our XRD and Raman facilities. After natural weathering, stibnite sulphur oxidize the Sb(III) depending of the pH to an Sb(V) oxyanion resulting in the transfer of Sb from the solid phase to the aqueous system (Adbel-Galil *et al*., 2015) As follows: $Sb(III)_2S_3 + 3H_2O + 6O_2 = 3SO_4^- + Sb(III)_2 + 6(H^+)$ and a second step as $Sb(III)_2O_3 + 3H_2O = 2Sb(V)O_3^- + 6(H+) + 4e^-$. Hence, environmental phases formed including Sb(V) speciation must contain H_2O and (OH) groups.

Laboratory driven experiments demonstrate as synthetic Sb metal reacts with oxygen to give a trivalent oxide, Sb_2O_3, a pentavalent oxide, Sb_2O_5, and also Sb_2O_4 with variable ratios of Sb^{3+} and Sb^{5+} ions. However, Sb in natural oxidized environments uses to be stable as Sb^{5+}. The relative concurrence of the XPS binding energy values of O_1s and $Sb3d_{5/2}$ photoemission peaks can be circumvented with mono-chromatized primary radiation and/or deconvolution software (Garbassi, 1980). The XPS data are compatible with the concurrence of Sb^{3+} and Sb^{5+} oxidation states in the "Cervantes" sample while they only show Sb^{5+} oxidation state in the "Brasina" sample.

Conclusions

Electronic images of yellow masses of Cervantes and Brasina specimens-type show microcrystalline phases with botryoidal textures and pockets characteristic of hydrous minerals which were crystallized from water solutions.

X-ray diffraction patterns of both powdered specimens-type match on several PDF-XRD cards of the Romeite sub-group included in the super-group of

minerals with pyrochlore structure. By micro-XRD we found more clusters of lewisite (7-66) in Cervantes samples and more clusters of stibiconite (10-388) and cervantite (11-694) in the Brasina samples.The EDS probes record accessorial amounts of Pb, As, Fe, P, Al and Cu elements and QEMSCAN minerals Sb-mineral, galena, muscovite, apatite, quartz and calcite. The EDS elemental analyses show antimony oxides with Ca: averaging circa 7% (Cervantes sample) and Ca averaging 2% (Brasina sample).

Cathodoluminescence spectra of Cervantes and Brasina type-samples show emissions at circa 311, 411, 473, 560, 624 and 660 nm characteristic of hydrous minerals with low luminescence emissions. The micro-Raman spectra of Cervantes yellowish specimens exhibit only a large peak at circa 517 cm^{-1} assigned to the SbO ν1 symmetric stretching mode as many other romeite, lewisite and synthetic Sb-oxides. The abundant presence of calcium, hydrous components and low crystallinity of sample are probably responsible of this simple spectrum. Conversely, Brasina specimen shows a complete Raman spectrum of Stibiconite with the characteristic main peak at 197 cm^{-1} is attributable to O-Sb-O bending modes together with other peaks at 522, 460, 400 and 142 cm^{-1}. This Raman spectrum with good matching to other published stibiconite-cervantite specimens could be explained since Brasina sample has less calcium and hydrous components. The Raman band at 1092 cm^{-1} associated to CO_3 group's vibration of calcium carbonates.

The FTIR spectra of both specimens-type are very similar including the broad band peaked at 3360 cm^{-1} (structural OH groups), 1638 cm^{-1} (molecular water), 1086 cm^{-1} (Sb-OH deformation) and 552 cm^{-1} (Sb-O deformation). Such spectra demonstrate clear presence of structural hydroxyl groups together with little amounts of bonded molecular water.

TG curves display total weight losses of 11% (Brasina) and 17% (Cervantes) attributable to thermal dehydration and dehydroxylation thermal mechanisms up to a complete decomposition of $Sb(OH)_5$ to Sb_2O_5 and H_2O. The possible weight gains when Sb^{3+} is oxidized to Sb^{5+} was not observed.

These conclusions suggest as both historical cervantite-type specimens are admixtures of hydrous Ca-Sb-romeite phases close to the isometric structure of pyrochlore and speciation Sb^{5+}. Furthermore, Cervantes and Brasina specimens shows minor differences among them concerning hydration wt.%, calcium wt.%, structure, Raman and cathodoluminescence spectra, and Sb speciation being probably hydroxycalciromeite (Cervantes) and admixtures hydroxycalciromeite and stibiromeite (Brasina). Under XPS, the speciation of both antimony ochres shows Sb^{3+} and Sb^{5+} in the Cervantes sample case but only Sb^{5+} in the Brasina case.

ACKNOWLEDGEMENTS

The authors gratefully acknowledged the financial support of the National Project PID2019-105469RB-C22 (Plan Estatal de Investigación Científica y Técnica y de Innovación Spain). Many thanks to technicians Maria Sanchez Arenillas (XPS), Rafael Gonzalez (XRD), Marta Furio (Raman), Cristina Paradela (DTA-TG), Dolores Gayo (FTIR), Manuel Linares (ESEM-EDS-CL) and Isabel Sanchez Almazo (FESEM-QUEMSCAN).

References

Abdel-Galil E.A.; El-Kenany W.M. & Hussin L.M.S. (2015). Preparation of nanostructured hydrated antimony oxide using a sol-gel process. Characterization and applications for sorption of La^{3+} and Sm^{3+} from aqueous solutions. Russian Journal of Applied Chemistry, 88(8): 1351-1360. https://doi:10.1134/S1070427215080200

Adelman, J.G.; Beauchemin, S.; Hendershot, W.H. & Kwong, Y.T.J. (2012). Change in the oxidation rate of stibnite as affected by pyrite in an oxygenated flow-through system. Geochemistry: Exploration, Environment, Analysis, 12: 227-239. https://doi.org/10.1144/1467-7873/11-RA-077

Ambe, S. (1987). Adsorption kinetics of antimony (V) ions onto α-Fe_2O_3 surfaces from an aqueous solution. Langmuir, 3(4): 489-493. https://doi.org/10.1021/la00076a009

Atencio D.; Andrade, M.B.; Christy, A.G.; Gieré, R. & Kartashow, P.M. (2010). The pyrochlore supergroup of minerals: nomenclature. Canadian Mineralogist, 48: 673-698. https://doi:10.3749/canmin.48.3.673.

Báez, D.F.; Pardo H.; Laborda I.; Marco J.F.; Yáñez C. & Bollo S. (2017). Reduced graphene oxides: Influence of the reduction method on the electrocatalytic effect towards nucleic acid oxidation. Nanomaterials, 7 (7): 168. https://doi.org/10.3390/nano7070168

Bahfenne S. & Frost R.L. (2010). Raman spectroscopic study of the antimonate mineral lewisite (Ca, Fe, $Na)_2(Sb,Ti)_2O_6(O, OH)_7$. Radiation Effects and

Defects in Solids, 165 (1): 46-53. https://doi.org/10.1080/10420150903418485

Bahfenne S. & Frost R.L. (2010). Vibrational Spectroscopic Study of the Antimonate Mineral Stibiconite. Spectroscopy Letters, 43 (6): 486-490. https://doi.org/10.1080/00387010903360313

Bahfenne S. & Frost R.L. (2010) Raman spectroscopic study of the antimonate mineral romeite. Spectrochimica Acta, Part A: Molecular and Biomolecular Spectroscopy, 75 (2): 637-639. https://doi:10.1016/j.saa.2009.11.031

Beudant F.S. (1837). Traité élémentaire de Minéralogie, 2nd edition, Carilian Jeune, Paris.

Biagioni C.; Orlandi P.; Nestola F. & Bianchin S. (2013). Oxycalcioroméite, $Ca_2Sb_2O_6O$, from Buca della Vena mine, Apuan Alps, Tuscany, Italy: a new member of the pyrochlore supergroup. Mineralogical Magazine, 77 (7): 3027-3037. https://doi.org/10.1180/minmag.2013.077.7.12

Birchall T.; Connor J.A. & Hillier I (1975). High-energy photoelectron spectroscopy of some antimony compounds. Journal of the Chemical Society, Dalton Transactions, 20: 2003-2006. https://doi:10.1039/DT9750002003

Bodenes L.; A. Darwiche, L. Monconduit & Martinez H. (2015).The Solid Electrolyte Interphase a key parameter of the high performance of Sb in sodium-ion batteries: Comparative x-ray photoelectron spectroscopy study of Sb/Na-ion and Sb/Li-ion batteries. Journal of Power Sources, 273: 14-24. https://doi.org/10.1016/j.jpowsour.2014.09.037

Botto, L.; Schalamuk, I.; Ametrano, S. & De Barrio, R. (1990). The vibrational spectrum of Cervantite (α-Sb_2O_4). Anales de la Asociación Química Argentina, 78 (4): 195-201.

Burke, E.A.J. (2006) A mass discreditation of GQN minerals. Canadian Mineralogist, 44: 1557-1560. https://doi:10.2113/gscanmin.44.6.1557

Cody C.A.; L. Dicarlo & Darlington R.K. (1979). Vibrational and Thermal Study of Antimony Oxides. Inorganic Chemistry, 18 (6): 1572-1576. https://doi/abs/10.1021/ic50196a036

Corby Anderson G. (2019). SME Mineral Processing and Extractive Metallurgy Handbook. Society for Mining, Metallurgy and Exploration, USA, 2203 pp.

Damour A. (1841). Sur la roméite, nouvelle espèce minérale, de St. Marcel, Piemont. Annales des Mines, 20 (3): 247-254. https://rruff.info/uploads/Annales_des_mines_20_1841_247.pdf

Dana J.D. (1850). A system of mineralogy: Comprising the most recent discoveries, 3rd edition. George P. Putnam, New York, London, 711 pp.

Delobel R.; H. Baussart & Leroy J.M. (1983). X-ray photoelectron spectroscopy study of uranium and antimony mixed metal-oxide catalysts. Journal of the Chemical Society, Faraday Transactions, 79: 879-891. https://doi:10.1039/f19837900879

Gadsden J.A. (1975). Infrared spectra of minerals and related inorganic compounds. Buttherworth & CO, London, 277 pp.

Garbassi F. (1980). XPS and AES Study of Antimony Oxides. Surface and interface analysis, 5(2): 165-169. https://doi.org/10.1002/sia.740020502

Garcia-Guinea J.; Garrido F.; López-Arce P.; Correcher V. & Delafiguera J. (2017). Spectral green cathodoluminescence emission from surfaces of insulators with metal-hydroxyl bonds. Journal of Luminescence, 190: 128-135. https://doi:10.1016/j.jlumin.2017.05.039

Garcia-Guinea J.; Correcher V.; Can N.; Garrido F. & Townsend P.D. (2018). Cathodoluminescence spectra recorded from surfaces of solids with hydrous molecules. Journal of Electron Spectroscopy and Related Phenomena, 227: 1-8. https://doi.org/10.1016/j.elspec.2018.05.008

Gilliam S.J.; Jensen J.O.; Banerjee A.; Zeroka D.; Kirkby S.J. & Merrow C.N. (2004). A theoretical and experimental study of Sb_4O_6: vibrational analysis, infrared and Raman spectra. Spectrochimica Acta Part A: Molecular Spectroscopy, 60: 425–434 https://doi:10.1016/s1386-1425(03)00245-2

Gottlieb P.; Wilkie G.; Sutherland D.; Ho-Tun E.; Suthers S.; Perera K.; Jenkins B.; Spencer S.; Butcher A. & Rayner J. (2000). Using quantitative electron microscopy for process mineralogy applications. The Journal of the Minerals, Metals and Materials Society, 52: 24–25 https://doi.org/10.1007/s11837-000-0126-9

Gründer W.; Pätzold H. & Strunz H. (1962). Sb_2O_4 als Mineral (Cervantit). Neues Jahrbuch für Mineralogie / Monatshefte, 5: 93-98.

Gunasekaran S, G. Anbalagan, G. & Pandi S. (2006). Raman and infrared spectra of carbonates of calcite structure. Journal of the Raman Spectroscopy, 37: 892–899 https://doi:10.1002/jrs.1518

Hussak E. & Prior G.T. (2018) Lewisite and zirkelite, two new Brazilian minerals. Mineralogical Magazine, 11: 80-88. https://doi.org/10.1180/minmag.1895.011.50.05

Izquierdo R.; Sacher E. & Yelon A. (1989). X-ray photoelectron spectra of antimony oxides. Applied Surface Science, 40: 175-177. https://doi.org/10.1016/0169-4332(89) 90173-6

Kharbish S. & Jelen S. (2016). Raman spectroscopy of the Pb-Sb sulfosalts minerals: Boulangerite, jamesonite, robinsonite and zinkenite. Vibrational

Spectroscopy, 85: 157-166. https://doi.org/10.1016/j.vibspec.2016.04.016

Li N.; Xia Y.; Mao Z.; Wang L.; Guan Y. & Zheng A. (2012) Influence of antimony oxide on flammability of polypropylene/intumescent flame retardant system. Polymer Degradation and Stability, 97(9): 1737-1744. https://doi.org/10.1016/j.polymdegradstab.2012.06.011

López G.P.; Castuer D.G. & Ratner B. (1991). XPS O1s binding energies for polymers containing hydroxyl, ether, ketone and ester groups. Surface and Interface Analysis, 17: 267-272. https://doi.org/10.1002/sia.740170508

Makreski P.; G. Petrusevski, S. Ugarkovic & G. Jovanovski (2013) Laser-induced transformation of stibnite (Sb_2S_3) and other structurally related salts. Vibrational Spectroscopy 68: 177-182. https://doi.org/10.1016/j.vibspec.2013.07.007

Marco J.F.; Gancedo J.R.; Ortiz J. & Gautier J.L. (2004). Characterization of the spinel-related oxides $NixCO_3-xO_4$ (x=0.3,1.3,1.8) prepared by spray pyrolysis at 350°C. Applied Surface Science, 227: 175-186. https://doi.org/10.1016/j.apsusc.2003.11.065

Meškinis S.; Vasiliauskas A.; Andrulevičius M.; Peckus D.; Tamulevičius S. & Viskontas K. (2020). Diamond like carbon films containing Si: Structure and nonlinear optical properties. Materials, 13 (4): 1-15. https://doi: 10.3390/ma13041003

Martín, J.D. (2006). XPowder: Programa para análisis cualitativo y cuantitativo por difracción de rayos X. Macla, 4: 35-44.

Miller, P.J. & Cody C.A. (1982). Infrared and Raman investigation of vitreous antimony trioxide. Spectrochimica Acta Part A: Molecular Spectroscopy, 38(5): 555-559 https://doi.org/10.1016/0584-8539(82)80146-3

Morgan W.E.; Stec, W.J. & Van Wazer J.R. (1973). Inner-orbital binding-energy shifts of antimony and bismuth compounds. Inorganic Chemistry, 12(4): 953–955. https://doi.org/10.1021/ic50122a054

Moulder J.F.; Stickle W.F.; Sobol P.E. & Bomben K.D. (1992) Handbook of X-ray Photoelectron Spectroscopy. Perkin-Elmer, Eden Prairie, USA, 261 pp.

Vitaliano C.J. & Mason B. (1952). Stibiconite and Cervantite. American Mineralogist, 37: 982-999. http://www.minsocam.org/ammin/AM37/AM37_982.pdf

Multani R.S.; Feldmann T. & Demopoulos G.P. (2016). Antimony in the metallurgical industry: A review of its chemistry and environmental stabilization options. Hydrometallurgy 164: 141-153. https://doi.org/10.1016/j.hydromet.2016.06.014.

Orecchio S. (2013) Micro-analytical characterization of decorations in handmade ancient floor tiles using inductively coupled plasma optical emission spectrometry (ICP-OES). Microchemical Journal, 108: 137-150. https://doi:10.1016/j.microc.2012.10.011

Rouse R.C.; Dunn P.J.; Peacor Dr. & Wang L. (1998), Structural studies of the natural antimonian pyrochlores. I. Mixed valency, cation site splitting, and symmetry reduction in lewisite. Journal of Solid State Chemistry, 141: 562-569. https://doi.org/10.1006/jssc.1998.8019

Schaller W.T. (1916). Mineralogical notes. Schneebergite and Romeite. U.S. Geological Survey Bulletin, 610: 81-95 https://pubs.usgs.gov/bul/0610/report.pdf

Fleischer M (1962). New mineral names. American Mineralogist, 47(9-10): 1216-1223.

Siebert H. (1959). Infrared spectra of telluric acids, tellurates and antimonates. Zeitschrift für anorganische und Allgemeine Chemie, 301: 161–170. https://doi.org/10.1002/zaac.19593010305

Smirnov M.Y.; A.V. Kalinkin & V.I. Bukhtiyarov (2007). X-ray photoelectron spectroscopic study of the interaction of supported metal catalysts with NOx. Journal of Structural Chemistry, 48: 1053–1060 https://doi.org/10.1007/s10947-007-0170-1

Stevens J.G.; Etter R.M. & Setzer E.W. (1993). ^{121}Sb Mössbauer spectroscopic study of the mineral stibiconite. Nuclear Instruments and Methods in Physics Research B, 76: 252-253. https://doi.org/10.1016/0168-583X(93)95199-F.

Stevens-Kalceff M.A. & Phillips M.R. (1995). Cathodoluminescence micro-characterization of the defect structure of quartz. Physical Review B., 52: 3122-3134 https://doi.org/10.1103/PhysRevB.52.3122

Wagner C.D.; Naumkin A.V.; Kraut-Vass A.; Allison J.W.; Powell C.J. & Rumble J.R. Jr. (2003) NIST Standard Reference Database 20, Version 3.4, web version. http:/srdata.nist.gov/xps/

Wilson S.C.; P.V. Lockwood, P.M. Ashley &Tighe M. (2010). The chemistry and behavior of antimony in the soil environment with comparisons to arsenic: A critical review. Environmental Pollution, 158 (5): 1169-1181, https://doi.org/10.1016/j.envpol.2009.10.045

Zubkova V.; D.Y. Pushcharowsky, D. Atencio, A.V. Arakcheeva & P.A. Matioli. (2000) The crystal structure of lewisite, $(Ca,Sb^{3+},Fe^{3+},Al,Na,Mn)_2(Sb^{5+},Ti)_2O_6(OH)$. Journal of Alloys and Compounds, 296: 75-79. https://doi.org/10.1016/S0925-8388(99)00513-7